

Simulated high-latitude soil thermal dynamics during the past four decades

Shushi Peng^{1,2}, Philippe Ciais², Gerhard Krinner¹, Tao Wang^{1,2}, Isabelle Gouttevin^{1,3}, A.
David McGuire⁴, David Lawrence⁵, Eleanor Burke⁶, Xiaodong Chen⁷, Bertrand Decharme⁸,
Charles Koven⁹, Andrew MacDougall¹⁰, Annette Rinke^{11,12}, Kazuyuki Saito¹³, Wenxin
Zhang¹⁴, Ramdane Alkama⁸, Theodore J. Bohn¹⁵, Christine Delire⁸, Tomohiro Hajima¹³,
Duoying Ji¹¹, Dennis P. Lettenmaier⁷, Paul A. Miller¹⁴, John C. Moore¹¹, Benjamin Smith¹⁴,
Tetsuo Sueyoshi^{16,13}

¹UJF – Grenoble 1/CNRS, Laboratoire de Glaciologie et Géophysique de l'Environnement
(LGGE), 38041 Grenoble, France

²Laboratoire des Sciences du Climat et de l'Environnement (LSCE), CEA-CNRS-UVSQ,
91191 Gif-sur-Yvette, France

³Irstea, UR HHLY, 5 rue de la Doua, CS 70077, 69626 Villeurbanne Cedex, France

⁴U.S. Geological Survey, Alaska Cooperative Fish and Wildlife Research Unit, University of
Alaska Fairbanks, Fairbanks, AK, USA

⁵National Center for Atmospheric Research, Boulder, CO, USA

⁶Met Office Hadley Centre, FitzRoy Road, Exeter, EX1 3PB, UK

⁷Department of Civil and Environmental Engineering, University of Washington, Seattle, WA,
USA

⁸CNRM-GAME, Unitémixte de recherche CNRS/Meteo-France (UMR 3589), 42 avCoriolis,
31057 Toulouse cedex, France

⁹Lawrence Berkeley National Laboratory, Berkeley, CA, USA

¹⁰School of Earth and Ocean Sciences, University of Victoria, Victoria, BC, Canada

¹¹College of Global Change and Earth System Science, Beijing Normal University, Beijing,
China

¹²Alfred Wegener Institute Helmholtz Centre for Polar and Marine Research, Potsdam,
Germany

¹³Research Institute for Global Change, Japan Agency for Marine-Earth Science and
Technology, Yokohama, Kanagawa, Japan

¹⁴Department of Physical Geography and Ecosystem Science, Lund University, Sölvegatan 12,
SE-223 62 Lund, Sweden

¹⁵School of Earth and Space Exploration, Arizona State University, Tempe, AZ, USA

¹⁶National Institute of Polar Research, Tachikawa, Tokyo, Japan

Revised Manuscript for *The Cryosphere*

Nov 22, 2015

392 words (abstract) + 5879 words (text) + 3 table + 9 figures + 62 references

***Corresponding author:**
Shushi Peng
LGGE/LSCE, France
Tel: +0033-1 69 08 53 03
Email: Shushi.Peng@lsce.ipsl.fr

Abstract

Soil temperature (T_s) change is a key indicator of the dynamics of permafrost. On seasonal and inter-annual time scales, the variability of T_s determines the active layer depth, which regulates hydrological soil properties and biogeochemical processes. On the multi-decadal scale, increasing T_s not only drives permafrost thaw/retreat, but can also trigger and accelerate the decomposition of soil organic carbon. The magnitude of permafrost carbon feedbacks is thus closely linked to the rate of change of soil thermal regimes. In this study, we used nine process-based ecosystem models with permafrost processes, all forced by different observation-based climate forcing during the period 1960-2000, to characterize the warming rate of T_s in permafrost regions. There is a large spread of T_s trends at 20 cm depth across the models, with trend values ranging from $0.010 \pm 0.003 \text{ } ^\circ\text{C yr}^{-1}$ to $0.031 \pm 0.005 \text{ } ^\circ\text{C yr}^{-1}$. Most models show smaller increase in T_s with increasing depth. Air temperature (T_a) and longwave downward radiation (LWDR) are the main drivers of T_s trends, but their relative contributions differ amongst the models. Different trends of LWDR used in the forcing of models can explain 61% of their differences in T_s trends, while trends of T_a only explain 5% of the differences in T_s trends. Uncertain climate forcing contributes a larger uncertainty in T_s trends ($0.021 \pm 0.008 \text{ } ^\circ\text{C yr}^{-1}$, mean \pm standard deviation) than the uncertainty of model structure ($0.012 \pm 0.001 \text{ } ^\circ\text{C yr}^{-1}$), diagnosed from the range of response between different models, normalized to the same forcing. In addition, the loss rate of near-surface permafrost area, defined as total area where the maximum seasonal active layer thickness (ALT) is less than 3 m loss rate is found to be significantly correlated with the magnitude of the trends of T_s at 1 m depth across the models ($R=-0.85$, $P=0.003$), but not with the initial total near-surface permafrost area ($R=-0.30$, $P=0.438$). The sensitivity of the total boreal near-surface permafrost area to T_s at 1 m, is estimated to be of $-2.80 \pm 0.67 \text{ million km}^2 \text{ } ^\circ\text{C}^{-1}$. Finally, by using two long-term LWDR datasets and relationships between trends of LWDR and T_s across

models, we infer an observation-constrained total boreal near-surface permafrost area decrease comprised between $39 \pm 14 \times 10^3$ and $75 \pm 14 \times 10^3 \text{ km}^2 \text{ yr}^{-1}$ from 1960 to 2000. This corresponds to 9% - 18% degradation of the current permafrost area.

Key words: soil temperature, permafrost, downward longwave radiation, climate warming, land surface model

1 Introduction

Arctic permafrost regions store ~1300 Pg carbon (C) in the soil, including ~1100 Pg C in frozen soil and deposits (Hugelius et al., 2014). Decomposition of these large carbon pools in response to permafrost thawing from projected future warming is expected to be a positive feedback on climate warming through increased emissions of CO₂ and CH₄ (Khvorostyanov et al., 2008; Schuur et al., 2008; McGuire et al., 2009; Koven et al., 2011; Schaefer et al., 2011). The magnitude of permafrost soil carbon feedbacks on climate depends on the rate of soil carbon decomposition, which is related to permafrost thaw, soil water and temperature changes, the quantity and quality of soil carbon available as a substrate for decomposition, and the concentration of oxygen in the soil, which determines CH₄ vs. CO₂ production ratio (Schuur et al., 2008; Schädel et al., 2014; Elberling et al., 2013). Both the rate of permafrost thaw and the rate of soil carbon decomposition are closely related to soil thermal dynamics (Koven et al., 2011; Schädel et al., 2014; Elberling et al., 2013).

Measurements of active layer depth across circumpolar regions and borehole temperature profiles indicate that active layer thickness on top of boreal permafrost has been increasing in response to the warming that occurred during recent decades in North America, Northern Europe and Russia (e.g. Zhang et al., 2001; Qian et al., 2011; Smith et al., 2005, 2010; Romanovsky et al., 2007, 2010). For example, the borehole record of Alert in Canada (82°30'N, 62°25'W) shows that soil temperature at 9 m, 15 m and 24 m increased at rates of 0.6 °C decade⁻¹, 0.4 °C decade⁻¹ and 0.2 °C decade⁻¹ from 1978 to 2007, respectively (Smith et al., 2012). These observations provide long-term local monitoring of changes in active layer thickness and soil temperature, but the measurement sites are sparse, and their temporal sampling frequency is often low (Romanovsky et al., 2010). Because site measurements cannot document permafrost area loss on a large scale, land surface models including 'cold

processes', such as soil freeze-thaw and the thermal and radiative properties of snow, are important tools for quantifying the rate of permafrost degradation on a large scale, and its evolution in response to climate change scenarios.

However, there are large uncertainties in soil thermal dynamics in land surface models (e.g. Koven et al., 2013), and these uncertainties also impact predictions of carbon-cycle feedbacks on climate. To quantify and reduce the uncertainty of modeled soil temperature (T_s), the driving factors of T_s trends need to be investigated. Besides the uncertainty in model parameterization and structure, the gridded climate forcing for offline land surface models over high latitude regions have large uncertainty (e.g. Troy and Wood, 2009; Rawlins et al., 2010). It is also important to distinguish the uncertainty caused by assigned parameter values and model structure from the uncertainty attributable to uncertain climate forcing data.

In this study, nine process-based models that participated in the Permafrost Carbon Network (PCN, www.permafrostcarbon.org) were used (1) to compare trends of simulated T_s at different depths over the boreal permafrost regions during the past four decades and to assess the uncertainty of modeled T_s trends; (2) to identify which factors drive trends of permafrost T_s ; and (3) to quantify the sensitivity of changes in near-surface permafrost area to warming.

2 Methods

2.1 Models and simulations

The nine land surface models that were used for simulating T_s in permafrost regions organized by Permafrost Carbon Network (PCN, www.permafrostcarbon.org) are listed in Table 1. All the models used finite difference solution of heat equation with phase change to simulate T_s , but models have different soil depths, snow parameterizations, and soil thermal

conductivities (Table 1). Three models (CLM, ISBA, UW-VIC) explicitly considered organic soil insulation and seven models explicitly considered the effect of water in soil on phase change. All models explicitly considered snow insulation but with different snow layers. The soil thermal conductivity depends on soil moisture in all models. More details can be found in Rawlins et al. (2015) and Koven et al. (2015). We defined the Northern Hemisphere permafrost spatial domain as the definition in Figure 1, and the analysis considers three permafrost regions, Boreal North America (BONA), Boreal Europe (BOEU), Boreal Asia (BOAS) (Figure 1; Brown et al., 1998). We did not include the Tibetan plateau because not all the models covered this region. Hereafter, the term “boreal regions” is used for the sum of the three sub-regions BONA, BOEU and BOAS in Figure 1.

Following the simulation protocol of the PCN project, nine land surface models performed historical simulations from 1960 to 2000, using different forcing data sets (Table 1). The different modeling groups in this study used different forcing datasets for climate and other model boundary conditions (Table 1), which collectively represent both uncertainty from climate forcing (and other forcing files) and from model parameterization and structure in simulating soil thermal dynamics across the permafrost region. Climate forcing data chosen by each group are presented in Table 1, and the differences in the trend of T_a , precipitation, and radiative forcing are summarized in Figure S1 and S2. How differences between these drivers are related to differences of the modeled T_s is discussed in the Results and Discussion section.

To separate the contributions of the trends of four forcing variables (T_a , atmospheric CO_2 , precipitation, and LWDR) on permafrost thermal dynamics and carbon stocks, six out of the nine models conducted factorial simulations (R01-R04). The ORCHIDEE and JULES

performed two additional simulations (R05-R06) to isolate the contribution of LWDR on T_s trends (Table 2 and 3). In the reference simulation R01, all drivers varied at the same time. In R02 T_a was detrended; in R03 atmospheric CO_2 was set constant to the observed 1960 level of 316 ppmv; In R04 both T_a and precipitation were detrended; in R05 T_a and LWDR were detrended; in R06 T_a , precipitation and LWDR were detrended. Differences between two simulations were used to separate the controlling effect of each driver on T_s . The interaction between CO_2 and T_a , precipitation such as enhanced vegetation growth by increased T_a /precipitation could loss less water under higher CO_2 condition, are also included in the differences between the two simulations.

2.2 Analysis

Modeled monthly T_s at 5, 20, 50, 100, 200 and 300 cm depths in every grid cell of each model were calculated by linear interpolation of T_s between the central depths of two adjacent layers. Modeled T_s at depths deeper than 300 cm (six models modeled T_s deeper than 300 cm, except CoLM, JULES and LPJ-GUESS) was not extrapolated (the maximum soil depth of each model is shown in Table 1). For each boreal sub-regions BONA, BOEU, BOAS (Figure 1) T_s was first averaged over all grid cells and the trend of regional mean T_s (denoted \dot{T}_s) was calculated from a linear regression. The statistical significance of \dot{T}_s is evaluated by a *t-test*.

To estimate the uncertainty of \dot{T}_s caused by differences in the trend of each climate input variable, we regressed \dot{T}_s against the trends of T_a , precipitation and short-wave downward radiation (SWDR) and LWDR, respectively, using the output of R01. The uncertainty of \dot{T}_s attributed to each forcing variable was defined as the resulting range of \dot{T}_s associated to

different trends in each forcing variable in the models. To achieve this aim, we regressed \dot{T}_s against forcing variable across the models, and the uncertainty of \dot{T}_s resulting from uncertain forcing data was calculated as the range of \dot{T}_s from the maximum and minimum values of forcing data in the regression equation. Then we define the \dot{T}_s uncertainty attributed to model structure, which reflects the differences in model parameterizations and parameter values, as the uncertainty of \dot{T}_s assuming all models were using the same climate forcing data.

Here, we defined near-surface permafrost as in previous studies (e.g. Schneider von Deimling et al., 2012): near-surface permafrost is defined as where the maximum seasonal thaw depth (i.e., the active layer thickness, ALT) is less than 3 m. The total near-surface permafrost area (NSPA) is the sum of the areas of grid cells that fulfill this condition.

We used monthly LWDR data from CRUNCEP v5.2 (<http://dods.extra.cea.fr/data/p529viov/cruncep>) and WATCH (Weedon et al., 2011) with a spatial resolution of 0.5° by 0.5° during the period 1960-2000 to derive the trend of LWDR. The CRUNCEP LWDR dataset was derived from CRU TS3.21 and NCEP reanalysis meteorology, and ancillary data sets (e.g. Wei et al., 2014). The WATCH LWDR dataset was derived from ERA-40 reanalysis (Weedon et al., 2011). Because there is no long-term large scale LWDR observation product available, we did an experiment using LWDR from CRUNCEP and WATCH data to estimate the loss of permafrost area during the period 1960-2000 by an empirical relationship between the loss of permafrost area and LWDR trends across the seven models out of the nine models (except LPJ-GUESS and UVic because LWDR was not used by these two models) (see section 3.4 below).

3 Results and Discussion

3.1 Trend in upper-layer soil temperature over boreal regions

The simulated values of \dot{T}_s at 20 cm depth averaged over boreal regions range from 0.010 ± 0.003 °C yr⁻¹ (CoLM) to 0.031 ± 0.005 °C yr⁻¹ (UVic) during the period 1960-2000 (Figure 2). Figure 3 shows \dot{T}_s at 20 cm for BONA, BOEU and BOAS regions. Six out of the nine models show the largest \dot{T}_s at 20 cm in BOAS, followed by BONA and BOEU. The other three models (CoLM, JULES and UW-VIC) show the smallest \dot{T}_s at 20 cm in BOAS. Among the six models with smaller \dot{T}_s at 20 cm in BOEU, we found that \dot{T}_s at 20 cm in BOEU is significantly lower than in BOAS and in BONA ($P < 0.001$, two sample *t-test*). This is also shown in the spatial distribution of \dot{T}_s at 20 cm (Figure 4). For example, in northern Siberia, T_s at 20 cm increased by more than 0.02 °C yr⁻¹ in five out of the nine models (ISBA, LPJ-GUESS, MICRO-ESM, ORCHIDEE and UVic) but decreased in two models (CoLM and JULES). All models show an increase of T_s at 20 cm in northern BONA, but this increase is of different magnitude between models (Figure 4). Six models show significant \dot{T}_s at 20 cm over northern and western Siberia, but all models show non-significant \dot{T}_s at 20 cm over northern BOEU (Figure 4).

3.2 Attenuation of the trend in soil temperature with soil depth

The trend of T_s at different soil depths is shown in Figure 5 for each model. Based on ground soil temperature observation, annual T_s at 1.6 m increased by 0.02 - 0.03 °C yr⁻¹ from 1960s to 2000s in Russia (Park et al., 2014). The simulated trends of T_s at 1.6 m over BOAS in most models are within this range (Figure S3). Two models (CoLM and JULES) show

vertically quasi-uniform \dot{T}_s over the upper 3 m of soil, probably because of too quick soil thermal equilibrium in these two models. The seven other models show decreasing values of \dot{T}_s with increasing soil depth, but the vertical gradient of \dot{T}_s varies among them (Figure 5a). UW-VIC has the largest negative vertical gradient of \dot{T}_s (-0.0052 ± 0.0001 °C yr⁻¹ m⁻¹), followed by ISBA, MICRO-ESM, ORCHIDEE and UVic ($\sim -0.0030 \pm 0.0003$ °C yr⁻¹ m⁻¹) and by near-zero vertical gradient of \dot{T}_s in CLM (-0.0009 ± 0.0003 °C yr⁻¹ m⁻¹) and in LPJ-GUESS (-0.0014 ± 0.0000 °C yr⁻¹ m⁻¹).

Figure 5b shows the trend of T_s in all soil layers over boreal regions. CLM and UVic show an increase of T_s even at depths deeper than 40m, but T_s exhibited no changes deeper than 22m in ORCHIDEE (Figure 5b). T_s increased in the deepest layer of ISBA (12m) and MIROC-ESM (14m), and the depth at which T_s exhibited no changes could not be deduced from these two models. UW-VIC shows a negative trend of T_s (i.e. cooling) at depths deeper than 2.5m, which may be related to higher soil heat capacities with increased soil moisture, resulting in cooler summertime soil temperatures and shallower active layers in the regions (Koven et al., 2015). The trends of T_s over BONA, BOEU and BOAS regions decrease in magnitude with increasing soil depth, but show different vertical gradients. In Figure S3, vertical gradient of \dot{T}_s is shown to be larger in BONA and BOAS than that in BOEU for most models. Figure 6 shows the spatial distribution of the difference in \dot{T}_s at depths between 0.2 m and 3 m. \dot{T}_s at 0.2m is larger than that at 3m over most regions in BONA, BOEU and BOAS in seven out of the nine models, except JULES and CoLM. Generally, borehole records show that mean annual soil temperature at depths between 10 m and 30 m have increased during the last three decades over the circumpolar northern permafrost regions

(Osterkamp, 2003; Romanovsky et al., 2010; Smith et al., 2005, 2012; Vaughan et al., 2013). In Alaska, T_s at 20 m from boreholes increased by ~ 1 °C between the early 1980s and 2001 (Osterkamp, 2003). The observed value of \dot{T}_s at one of Alert (BH3) boreholes is of ~ 0.04 °C yr^{-1} at ~ 2.5 m depth and nearly zero at ~ 27 m depth during the period 1979-2004 (see Figure 9 in Smith et al., 2012). Some boreholes (BH1 and BH2) at Alert however still indicated a small warming during the period 1979-2008 (Smith et al., 2012) at 37m. This suggests that much deeper maximum soil depth than the currently prescribed maximum soil depths (Table 1) are needed for some models to calculate the heat flux into the entire soil profile (Stevens et al., 2007). CoLM, JULES and LPJ-GUESS have too shallow maximum soil depth for the calculation of permafrost soil temperature trends over the last four decades, which makes these models even less realistic for deeper T_s projections over the next century (e.g. Alexeev et al., 2007). Compared to the increased ground temperature at depths deeper than 20 m in boreholes during the past three decades (Vaughan et al., 2013), most models that do not have deeper soil depth seem to underestimate the penetration of heat into deep soil layers (Figure 5b). For the bottom boundary geothermal heat flux, eight out of the nine model assumes to be zero. The ignored boundary geothermal heat flux is valid for the upper 20-30 m of soil within century scale (Nicolovsky et al., 2007), but for millennium or longer glacial-interglacial cycle permafrost simulation, the bottom boundary geothermal heat flux should not be ignored. Note that this comparison may be biased because of different periods and climate records between sites and model grid cells. It is also recommended that simulations at site level using in-situ local climate forcing can be compared with temperature profiles of boreholes (Smith et al., 2012) to evaluate why models underestimate the warming of T_s at deeper depths.

3.3 Drivers of trend in soil temperature

We used the sensitivity runs (R02-R06) compared with the reference simulation with all

drivers varying together (R01) to separate the effects of T_a , CO_2 , precipitation, and LWDR on \dot{T}_s during 1960-2000 (Table 3). Seven of the nine models only provided results from R02, R03 and R04. Except for JULES, all the models show a positive response of T_s to increasing T_a , but with different sensitivities (Table 3). The fraction of the trend of T_s explained by air temperature increase alone (R01 – R02) is nearly 100% in CLM, ISBA and more than 100% in UW-VIC, against only 34%, 56% and 67% in ORCHIDEE, UVic and LPJ-GUESS. This indicates the importance of increasing T_a on the trend of T_s , and is consistent with observations. Based on 30 climate stations observations in Canada during the period 1958-2008, T_s at 10 cm significantly and positively correlates with T_a at most sites (>90%) in spring, but at fewer sites (<30%) in winter (Qian et al., 2011). For winter T_s , the winter snow depth was found to have significant and positive correlation with T_s in shallow soil layers (e.g. Zhang et al., 2001; Qian et al., 2011). Recent increases in T_a also explain the trend of T_s at 1.6m measured at Churapcha metrological station (N62.02, E132.36), and at 5 m measured in a borehole at Iqaluit (N63.47, W68.48) in Canada (Smith et al., 2005; Romanovsky et al., 2007). To some extent, the trend of T_a is a good indicator for the trend of deep permafrost ground temperature with some time lag (Romanovsky et al., 2007). For the modeled T_s in land surface models, the effects of T_a on T_s depend on surface energy balance and ground heat flux into soil; i.e. the extent of coupled T_a on T_s relates to the surface properties such as snow, organic soil horizons and roughness etc. in the models. The different relative contributions of the trend of T_a to the trend of T_s in these models maybe mainly result from the different model parameterization and structures, as the trends of T_a (~ 0.03 °C yr⁻¹) in the climate forcing do not have a large spread (Figure 7).

The increase of atmospheric CO_2 concentration has almost no effect on the increase of T_s in most models (-5% to +4% of increase of T_s , Table 3). This is expected since CO_2 has no

direct effect on T_s apart from its impact on climate. The only indirect effect of rising CO_2 on T_s trends could result from feedbacks between plant productivity driven by rising CO_2 , soil carbon changes and soil thermal properties. For instance, if models include heat production from microbial decomposition of soil organic carbon (Khvorostyanov et al., 2008) or if changes in soil organic carbon from the balance of NPP input and decomposition, these could impact the soil temperature directly or the profile of soil heat conductivity and capacity. In that case, the expected response is that a CO_2 driven increase of productivity will increase soil organic carbon, which will enhance the insulation effect of soil organic carbon in the soil and lower the trend of T_s (Lawrence et al., 2008; Lawrence and Slater, 2008; Koven et al., 2009). Further, complex changes in the surface energy balance from changes in evapotranspiration under higher CO_2 concentrations can influence soil moisture content and affect T_s trends (e.g. Field et al., 1995). Most models do not have a feedback between soil organic carbon dynamics and soil thermal properties, and the increase in soil organic carbon due to rising CO_2 is relatively small in the models compared to the initial soil organic carbon storage ($< 0.1\%$). The changes in evapotranspiration because of increasing CO_2 are also relatively small (-3% to $+1\%$). Therefore, the increased CO_2 concentration has a very small effect on \dot{T}_s from 1960 to 2000.

Precipitation shows an increase in BONA and BOEU and a decrease in BOAS in the climate forcing used by most models (Figure S1b). None of the trends of boreal precipitation are significant ($P > 0.05$; except for the UW-VIC and JULES drivers). Changes in precipitation alone (R02 – R04) are found to cause a negative trend of T_s in CLM, JULES and UW-VIC, no effects in LPJ-GUESS and UVic, and a positive trend in ISBA and ORCHIDEE (Table 3). Increasing winter snowfall can enhance T_s in winter through snow insulation effect (e.g. Smith et al., 2010; Koven et al., 2013). All models in this study indeed show higher winter T_s

where winter snow depth became deeper, but with different magnitudes of snow insulation effects across the models. The snow insulation effects are smaller in ISBA, LPJ-GUESS and UVic than that in the other models. A decrease in snowfall could contribute a negative trend of T_s in CLM, and an increase in snowfall could enhance T_s in ORCHIDEE (Figure S4; Table 3). In addition, increased rainfall in summer can cause an increase in evapotranspiration during the growing seasons, which could depress the increase of T_s . The effects of snowfall trends and growing season precipitation trends may oppose each other as mentioned above. These two contrasting effects cannot be separated in this analysis, because models did not run simulations with seasonally detrended precipitation. But the different effects of seasonal precipitation on T_s should be studied in the future.

LWDR significantly increased since 1960 in all models yet with different trends in the forcing data used by each modeling group ($0.058 \sim 0.200 \text{ W m}^{-2} \text{ yr}^{-1}$) (Figure S2a). LWDR forcing is mainly from two reanalysis datasets (ERA and NCEP) with corrections (e.g. Weedon et al., 2011; <http://dods.extra.cea.fr/data/p529viov/cruncep>). ORCHIDEE and JULES performed the simulation R05 with detrended LWDR. The results of R02 – R05 allowing to attribute \dot{T}_s to trends of LWDR, indicate that the increase of LWDR explains 56% and 31% of the trend of T_s since 1960 in ORCHIDEE and JULES, respectively. Increased LWDR provides additional energy to the surface, and dominates the atmosphere-to-soil energy flux in winter over boreal regions when shortwave radiation is small. Even in summer, LWDR contributes ~60% of total downward radiation (SWDR+LWDR) over boreal regions in CRUNCEP. An increase of LWDR with time thus increases the surface energy input, which accelerates the warming of T_s in case the extra energy is not dissipated by an increase of sensible and latent heat flux. The contribution of changes in LWDR, T_a and other factors on all components of the surface energy budget and on T_s could be further studied by testing

models against observations from eddy-flux towers located in permafrost soils.

3.4 Uncertainty of modeled soil temperature trends

The uncertainty of modeled \dot{T}_s at 20 cm is large, as given by the spread of model results (0.010 °C yr⁻¹ - 0.031 °C yr⁻¹). The uncertainty of \dot{T}_s across the models can be conceptually decomposed into two components, a forcing uncertainty (FU) reflecting how different climate input data used by each modeling group contribute to the spread of \dot{T}_s (Table 1), and a structural uncertainty (SU) related to uncertain parameter values and different equations and parameterizations of processes in models. Since T_a and LWDR are the two main drivers of the increase of T_s in most of the models (Section 3.3), we regressed \dot{T}_s during 1960-2000 against the trends of T_a and LWDR, in order to estimate the FU. We then estimated SU from the uncertainty of parameters in the regression equation for a normalized same climate forcing across all models.

We found no significant correlation between \dot{T}_a and \dot{T}_s over boreal regions or sub-regions across the nine models (Figure 7 and Figure S5), indicating that a bias of \dot{T}_a forcing is not simply associated with the bias of \dot{T}_s in a particular model compared to the others. We also found that trends of SWDR and precipitation do not significantly explain differences in \dot{T}_s at 20 cm across the models ($P > 0.05$; 21% and 19% explanation of differences in \dot{T}_s at 20 cm for trends of SWDR and precipitation respectively; Figure S6). The correlations between trends in winter snowfall and trends of annual or winter T_s at 20 cm are not significant ($P > 0.05$) across the models for boreal regions or sub-regions. However, the

373 trend of LWDR ($L\dot{W}DR$) can explain 61% of the differences in \dot{T}_s at 20 cm across the
 374 models (Figure 8). This result indicates that, across the model ensemble, differences of \dot{T}_s at
 375 20 cm between models are positively correlated ($R=0.78$, $P=0.037$) with differences of
 376 $L\dot{W}DR$ used by the different modeling groups. \dot{T}_s at 1 m also significantly correlated with
 377 $L\dot{W}DR$ ($R=0.79$, $P=0.034$) across the models. The values of $L\dot{W}DR$ used by different
 378 models averaged over permafrost regions, range from $0.058 \text{ W m}^{-2} \text{ yr}^{-1}$ to $0.200 \text{ W m}^{-2} \text{ yr}^{-1}$,
 379 statistically explaining a range of simulated \dot{T}_s at 20 cm of $0.021 \pm 0.005 \text{ }^\circ\text{C yr}^{-1}$ (solid blue
 380 arrow in Figure 8). This \dot{T}_s range defines the FU (the range of \dot{T}_s to $L\dot{W}DR$ from 0.058
 381 $\text{W m}^{-2} \text{ yr}^{-1}$ to $0.200 \text{ W m}^{-2} \text{ yr}^{-1}$ based on the linear regression of Figure 8). We also used
 382 multiple linear regression between \dot{T}_s at 20 cm depth and \dot{T}_a , $L\dot{W}DR$ as independent
 383 variables across the models, to derive an estimation of the FU on \dot{T}_s of $0.021 \pm 0.008 \text{ }^\circ\text{C yr}^{-1}$
 384 (the deviation was derived from the uncertainty of regression coefficients in the multiple
 385 linear regression). However, the uncertainty of the linear regression of \dot{T}_s at 20 cm by
 386 $L\dot{W}DR$ or \dot{T}_a and $L\dot{W}DR$ shows that if all the models used the same climate forcing
 387 data, the SU would be of $0.012 \pm 0.001 \text{ }^\circ\text{C yr}^{-1}$ (solid orange arrow in Figure 8). If all models
 388 used LWDR from CRUNCEP or WATCH, then applying the trend of annual LWDR ($0.087 \pm$
 389 $0.023 \text{ W m}^{-2} \text{ yr}^{-1}$ from CRUNCEP and $0.187 \pm 0.028 \text{ W m}^{-2} \text{ yr}^{-1}$ from WATCH) during the
 390 period 1960-2000 as an emerging observation constraint empirical relationship in Figure 8,
 391 the posterior range is reduced compared with the prior \dot{T}_s range (black curve in right panel
 392 of Figure 8). Overall, the total uncertainty range of \dot{T}_s at 20 cm ($\sim 0.02 \text{ }^\circ\text{C yr}^{-1}$, defined as the
 393 spread of \dot{T}_s at 20 cm across the models) can be broken down into FU ($0.021 \pm 0.008 \text{ }^\circ\text{C yr}^{-1}$)

and SU ($0.012 \pm 0.001 \text{ }^{\circ}\text{C yr}^{-1}$). Since FU and SU are not independent, the total uncertainty of \dot{T}_s at 20 cm is not the sum of FU and SU.

Further, we found that correlation coefficients between trends of summer T_s at 20 cm and at 1 m and summer LWDR over boreal regions are statistically significant ($P < 0.05$) (Figure S7). This is also found for winter (November to March) T_s at 20 cm and 1 m (Figure S8). Trends of summer and winter T_s at 20 cm or 1 m are not significantly correlated with other climate drivers than LWDR (snowfall, rainfall, T_a and SWDR) across the models ($P > 0.05$).

Meteorological stations are sparse in the cold permafrost regions. For example, there are only 8.8 stations per million km^2 north of 60°N in the CRU TS3.22 gridded air temperature product compared to 41.1 stations per million km^2 between 25°N and 60°N . This results in uncertainty in gridded climate products over Arctic regions, especially for trends of Arctic climate variables (Mitchell and Jones, 2005; Troy and Wood, 2009; Rawlins et al., 2010; Weedon et al., 2011). Troy and Wood (2009) reported 15-20 W m^{-2} of differences in radiative fluxes on seasonal timescales over northern Eurasia, between six gridded products. Between different gridded observations and reanalysis precipitation products, the magnitude of Arctic precipitation ranges from 410 mm yr^{-1} to 520 mm yr^{-1} , and the trend of Arctic precipitation also has a large spread (Rawlins et al., 2010). These large uncertainties in climate forcing in Arctic undoubtedly can cause large spread of modeled T_s . We found that the FU dominates the total uncertainty of \dot{T}_s . This suggests that modelers not only need to improve their models, but also need better climate forcing data (or need to test the effects of different climate input data) when modeling long term changes of T_s in permafrost regions. However, to quantify the SU, simulations using the same agreed upon climate forcing data are highly recommended to further attribute the contribution of each process in the soil thermal

dynamics of models such as organic carbon insulation effects, snow insulation effects, latent heat formation and emission, soil conductivity and surface properties (see Lawrence and Slater, 2008; Koven et al., 2009; Bonfils et al., 2012; Gouttevin et al., 2012). In addition, important processes in permafrost regions such as dynamics of excessive ground ice (e.g. ice wedge growth and degradation) and thermokarst lakes (formation, expansion and drainage) should be developed and evaluated in land surface models to improve the prediction of future permafrost feedbacks (e.g. van Huissteden et al., 2013; Lee et al., 2014).

3.5 Emerging constraint on how much near-surface permafrost has disappeared.

The total boreal NSPA during 1960-2000 estimated by the nine models ranges from 6.8 million km² (CoLM) to 19.7 million km² (ORCHIDEE). The average of total NSPA in the nine models ensemble (12.5 million km²) is smaller than the estimate from the International Permafrost Association (IPA) map (16.2 million km²; Brown et al, 1998; Slater and Lawrence et al., 2013). A statistic model based on relationships between air temperature and permafrost shows that permafrost extent over Northern Hemisphere was also estimated in the range 12.9 - 17.8 million km² (Gruber, 2012), and six out of the nine models are within this range. Eight out of the nine models show a significant decrease in NSPA with climate warming during 1960-2000 (except UW-VIC). The loss rate of NSPA is found to vary by a factor of 13 across the nine models, varying from $-4 \times 10^3 \text{ km}^2 \text{ yr}^{-1}$ in MIROC-ESM to $-50 \times 10^3 \text{ km}^2 \text{ yr}^{-1}$ in JULES (Figure 9a). The average of loss rate of NSPA across the models ($-23 \pm 23 \times 10^3 \text{ km}^2 \text{ yr}^{-1}$) is smaller than in the previous estimations of Burke et al. (2013) and Slater and Lawrence (2013). For example, the loss rate of NSPA was estimated at $-81 \times 10^3 - -55 \times 10^3 \text{ km}^2 \text{ yr}^{-1}$ during the period 1967-2000 by JULES offline simulations with different climate forcing datasets (Burke et al., 2013). The ranges of loss rate of NSPA in BONA, BOEU and BOAS across the models are $-16.6 \times 10^3 - 2.2 \times 10^3 \text{ km}^2 \text{ yr}^{-1}$, $-4.0 \times 10^3 - 0.0 \times 10^3 \text{ km}^2 \text{ yr}^{-1}$ and

-34.2×10³ – -1.1×10³ km² yr⁻¹, respectively (Figure 9). This is consistent with the observed permafrost degradation (decrease in thickness) in these regions (Vaughan et al., 2013).

The retreat rate of NSPA is not correlated significantly with the initial NSPA of each model (R=-0.30, P=0.438), implying that the initial state of models is less important than their response to climate change in determining NSPA loss rates. On the contrary to the small effect of initial NSPA, the trend of summer T_s at 1 m is found to be strongly correlated with NSPA loss rates across the models of the ensemble. Figure 9 shows that the trend of summer T_s at 1 m can explain 73% of the differences in NSPA loss rates between models. The sensitivity of NSPA loss rate to summer \dot{T}_s at 1 m is estimated to be -2.80 ± 0.67 million km² °C⁻¹, based on the linear regression between the loss rate of NSPA and the trend of summer T_s at 1 m across the nine models (Figure 9). For the BONA, BOEU and BOAS sub-regions, the sensitivities of NSPA loss rate to summer \dot{T}_s at 1 m are -0.74 ± 0.10 million km² °C⁻¹, -0.09 ± 0.03 million km² °C⁻¹ and -1.74 ± 0.59 million km² °C⁻¹, respectively (Figure 9). The sensitivity of future total NSPA changes to T_a over Pan-Arctic regions was estimated to be -1.67 ± 0.7 million km² °C⁻¹, ranging from 0.2 million km² °C⁻¹ to 3.5 million km² °C⁻¹ in CMIP5 model ensembles (Slater and Lawrence, 2013; Koven et al., 2013). The average of trends in summer T_s at 1 m is only 70% (43%-100%) of \dot{T}_a in the nine models, so that the sensitivity of total NSPA to T_a over boreal regions in the nine models is about -2.00 ± 0.47 million km² °C⁻¹, which is larger than that from CMIP5 model ensemble, but comparable within the uncertainties of each estimate (Slater and Lawrence, 2013). Six out of the nine models of this study were also used as land surface schemes of the coupled CMIP5 models, but possibly for different versions.

A mean positive trend of summer LWDR of $0.073 \pm 0.030 \text{ W m}^2 \text{ yr}^{-1}$ and 0.210 ± 0.027
 $\text{W m}^2 \text{ yr}^{-1}$ over boreal regions from 1960 to 2000 are derived from the CRUNCEP and
 WATCH datasets respectively. We applied this trend of LWDR to an emerging constraint on
 summer T_s trends from the relationship between the trend of summer LWDR and the trend of
 summer T_s at 1 m (Figure S7). This approach constrains the trend of summer T_s to $0.014 \pm$
 $0.004 \text{ }^\circ\text{C yr}^{-1}$ with CRUNCEP and to $0.027 \pm 0.004 \text{ }^\circ\text{C yr}^{-1}$ with WATCH. The uncertainty is
 reduced by 50% from the prior range including different models and different forcings. A total
 NSPA loss rate of $39 \pm 14 \times 10^3 \text{ km}^2 \text{ yr}^{-1}$ can be constrained by multiplying the sensitivity of
 total NSPA loss rate to summer \dot{T}_s at 1 m ($-2.80 \pm 0.67 \text{ million km}^2 \text{ }^\circ\text{C}^{-1}$) by the trend of T_s
 at 1 m itself empirically estimated by \dot{LWDR} during 1960-2000 from CRUNCEP ($0.014 \pm$
 $0.004 \text{ }^\circ\text{C yr}^{-1}$). The constrained loss rate of NSPA over BONA, BOEU and BOAS based upon
 the CRUNCEP \dot{LWDR} from 1960 to 2000 are $11 \pm 5 \times 10^3 \text{ km}^2 \text{ yr}^{-1}$, $1 \pm 1 \times 10^3 \text{ km}^2 \text{ yr}^{-1}$
 and $25 \pm 11 \times 10^3 \text{ km}^2 \text{ yr}^{-1}$, respectively. Similarly, if WATCH \dot{LWDR} is used to constrain
 NSPA loss rate, the total NSPA loss rate is $75 \pm 14 \times 10^3 \text{ km}^2 \text{ yr}^{-1}$, and loss rate of NSPA over
 BONA, BOEU and BOAS are estimated to be $28 \pm 10 \times 10^3 \text{ km}^2 \text{ yr}^{-1}$, $2 \pm 1 \times 10^3 \text{ km}^2 \text{ yr}^{-1}$ and
 $39 \pm 19 \times 10^3 \text{ km}^2 \text{ yr}^{-1}$, respectively. The southern boundary of the discontinuous permafrost
 zone has been observed to shift northward during the recent decades (Vaughan et al., 2013),
 which is generally consistent with the simulations reported in this study. The larger warming
 rate and higher sensitivity of NSPA loss to T_s over BOAS could explain the reason for
 significant degradation of permafrost over BOAS than the other boreal regions (Vaughan et al.,
 2013). The larger permafrost degradation rate in BOAS than that in BONA may have larger
 effects on changes in vegetation distribution and growth, and permafrost carbon in these two
 regions, and can be quantified in future studies. Obviously, there is a large difference in
 constrained NSPA between CRUNCEP and WATCH. In the future, long-term climate

reanalysis including radiation evaluated against sites with long-term radiation measurements (<http://www.geba.ethz.ch>) would be extremely useful for land surface models to provide improved estimate of NSPA.

4 Conclusions

In this study, trends of soil temperature (T_s) over boreal regions from nine process-based models were analyzed for the past 40 years. All models produce a warming of T_s , but the trends of T_s at 20 cm depth range from $0.010 \pm 0.003 \text{ }^\circ\text{C yr}^{-1}$ (CoLM) to $0.031 \pm 0.005 \text{ }^\circ\text{C yr}^{-1}$ (UVic) during 1960-2000. Most models show a smaller increase of T_s with deeper depth. Air temperature (T_a) and longwave downward radiation (LWDR) are found to be the predominant drivers of the increase in T_s averaged across large spatial scales. The relative contribution of T_a and LWDR trends to the increase of T_s is however different across the models. Note that the relative contribution of LWDR is based on only two models in this study, and this needs further investigation. The total uncertainty of the trend of T_s at 20 cm is decomposed into the uncertainty contributed by uncertain climate forcing datasets ($0.021 \pm 0.008 \text{ }^\circ\text{C yr}^{-1}$) and the uncertainty reflecting model structure ($0.012 \pm 0.001 \text{ }^\circ\text{C yr}^{-1}$). The near-surface permafrost area (NSPA) loss rate is significantly correlated among the model results with the simulated trend of T_s at 1 m, with a linear sensitivity of total NSPA loss rate to summer trend of T_s (\dot{T}_s) at 1 m of $-2.80 \pm 0.67 \text{ million km}^2 \text{ }^\circ\text{C}^{-1}$. Based on LWDR from CRUNCEP and WATCH data, the total NSPA decrease is estimated to be $39 \pm 14 \times 10^3 \text{ km}^2 \text{ yr}^{-1}$ - $75 \pm 14 \times 10^3 \text{ km}^2 \text{ yr}^{-1}$ from 1960 to 2000. The constraint method used in this study could be applied to estimate historical and future permafrost degradation rate, and further to quantify the permafrost carbon loss by permafrost carbon distribution map.

Given that meteorological stations are sparse in the cold permafrost regions, especially in

Siberia and other unpopulated land in the north, the gridded climate products over high-latitude regions have a large uncertainty as well (Mitchell and Jones, 2005; Rawlins et al., 2010; Weedon et al., 2011). This large uncertainty could propagate into simulated permafrost dynamics and feedbacks. More sites are needed in high-latitude regions for reducing the climate uncertainty. Future model inter-comparisons on permafrost dynamics should investigate the full uncertainty by conducting simulations for multiple climate forcing data sets. Since the beginning of the satellite era, microwave emissivity data related to land surface temperature has become increasingly available (e.g. Smith et al., 2004). These images could be used to independently evaluate soil surface temperature in models on a large scale or be integrated in ground temperature models (e.g. Westermann et al., 2015), although they have their own uncertainties. In addition, many complex processes affect permafrost thermal dynamics in the models, such as soil organic insulation effects, snow insulation effects, soil freeze-thaw etc., it is valuable to evaluate the uncertainty of each process effects on soil thermal dynamics simulations based on site measurements. This could be helpful for reducing permafrost simulation uncertainty.

Acknowledgments

This study has been supported by the PAGE21 project, funded by the European Commission FP7-ENV-2011 (grant agreement NO. 282700) and has been developed as part of the modeling integration team of the Permafrost Carbon Network (PCN, www.permafrostcarbon.org) funded by the National Science Foundation. Any use of trade, firm, or product names is for descriptive purposes only and does not imply endorsement by the U.S. Government. Bertrand Decharme and Christine Delire were supported by the French Agence Nationale de la Recherche under agreement ANR-10-CEPL-012-03.

542

543 **References**

- 544 Adam, J. C., Clark, E. A., Lettenmaier, D. P., and Wood, E. F.: Correction of Global
545 Precipitation Products for Orographic Effects, *Journal of Climate*, 19, 15-38,
546 doi:10.1175/jcli3604.1, 2006.
- 547 Alexeev, V. A., Nicolsky, D. J., Romanovsky, V. E., and Lawrence, D. M.: An evaluation of
548 deep soil configurations in the CLM3 for improved representation of permafrost,
549 *Geophysical Research Letters*, 34, L09502, doi:10.1029/2007gl029536, 2007.
- 550 Avis, C. A., Weaver, A. J., and Meissner, K. J.: Reduction in areal extent of high-latitude
551 wetlands in response to permafrost thaw, *Nature Geosci*, 4, 444-448, 2011.
- 552 Best, M. J., Pryor, M., Clark, D. B., Rooney, G. G., Essery, R. L. H., Ménard, C. B., Edwards,
553 J. M., Hendry, M. A., Porson, A., Gedney, N., Mercado, L. M., Sitch, S., Blyth, E.,
554 Boucher, O., Cox, P. M., Grimmond, C. S. B., and Harding, R. J.: The Joint UK Land
555 Environment Simulator (JULES), model description – Part 1: Energy and water fluxes,
556 *Geosci. Model Dev.*, 4, 677-699, doi:10.5194/gmd-4-677-2011, 2011.
- 557 Bohn, T. J., Podest, E., Schroeder, R., Pinto, N., McDonald, K. C., Glagolev, M., Filippov, I.,
558 Maksyutov, S., Heimann, M., Chen, X., and Lettenmaier, D. P.: Modeling the large-scale
559 effects of surface moisture heterogeneity on wetland carbon fluxes in the West Siberian
560 Lowland, *Biogeosciences*, 10, 6559-6576, doi:10.5194/bg-10-6559-2013, 2013.
- 561 Bonfils, C. J. W., Phillips, T. J., Lawrence, D. M., Cameron-Smith, P., Riley, W. J., and Subin,
562 Z. M.: On the influence of shrub height and expansion on northern high latitude climate,
563 *Environmental Research Letters*, 7, 015503, doi:10.1088/1748-9326/7/1/015503, 2012.
- 564 Brown, J., Ferrians, O.J.Jr., Heginbottom, J.A.. and Melnikov, E.S. (1998, revised February
565 2001). Circum-Arctic map of permafrost and ground-ice conditions. Boulder, CO:
566 National Snow and Ice Data Center/World Data Center for Glaciology. Digital Media.

567 Burke, E., Dankers, R., Jones, C., and Wiltshire, A.: A retrospective analysis of pan Arctic
 568 permafrost using the JULES land surface model, *Clim Dyn*, 41, 1025-1038,
 569 doi:10.1007/s00382-012-1648-x, 2013.

570 Clark, D. B., Mercado, L. M., Sitch, S., Jones, C. D., Gedney, N., Best, M. J., Pryor, M.,
 571 Rooney, G. G., Essery, R. L. H., Blyth, E., Boucher, O., Harding, R. J., Huntingford, C.,
 572 and Cox, P. M.: The Joint UK Land Environment Simulator (JULES), model description
 573 – Part 2: Carbon fluxes and vegetation dynamics, *Geosci. Model Dev.*, 4, 701-722,
 574 doi:10.5194/gmd-4-701-2011, 2011.

575 Dai, Y., Zeng, X., Dickinson, R. E., Baker, I., Bonan, G. B., Bosilovich, M. G., Denning, A. S.,
 576 Dirmeyer, P. A., Houser, P. R., Niu, G., Oleson, K. W., Schlosser, C. A., and Yang, Z.-L.:
 577 The Common Land Model, *Bulletin of the American Meteorological Society*, 84,
 578 1013-1023, doi:10.1175/bams-84-8-1013, 2003.

579 Dai, Y., Dickinson, R. E., and Wang, Y.-P.: A Two-Big-Leaf Model for Canopy Temperature,
 580 Photosynthesis, and Stomatal Conductance, *Journal of Climate*, 17, 2281-2299,
 581 doi:10.1175/1520-0442(2004)017<2281:atmfct>2.0.co;2, 2004.

582 Decharme, B., Boone, A., Delire, C., and Noilhan, J.: Local evaluation of the Interaction
 583 between Soil Biosphere Atmosphere soil multilayer diffusion scheme using four
 584 pedotransfer functions, *Journal of Geophysical Research: Atmospheres*, 116, D20126,
 585 doi:10.1029/2011jd016002, 2011.

586 Decharme, B., Martin, E., and Faroux, S.: Reconciling soil thermal and hydrological lower
 587 boundary conditions in land surface models, *Journal of Geophysical Research:*
 588 *Atmospheres*, 118, 7819-7834, doi:10.1002/jgrd.50631, 2013.

589 Elberling, B., Michelsen, A., Schadel, C., Schuur, E. A. G., Christiansen, H. H., Berg, L.,
 590 Tamstorf, M. P., and Sigsgaard, C.: Long-term CO₂ production following permafrost
 591 thaw, *Nature Clim. Change*, 3, 890-894, doi:10.1038/nclimate1955, 2013.

- Field, C. B., Jackson, R. B., and Mooney, H. A.: Stomatal responses to increased CO₂: implications from the plant to the global scale, *Plant, Cell & Environment*, 18, 1214-1225, doi:10.1111/j.1365-3040.1995.tb00630.x, 1995.
- Gouttevin, I., Krinner, G., Ciais, P., Polcher, J., and Legout, C.: Multi-scale validation of a new soil freezing scheme for a land-surface model with physically-based hydrology, *The Cryosphere*, 6, 407-430, doi:10.5194/tc-6-407-2012, 2012.
- Gruber, S.: Derivation and analysis of a high-resolution estimate of global permafrost zonation, *The Cryosphere*, 6, 221-233, doi:10.5194/tc-6-221-2012, 2012.
- Harris, I., Jones, P. D., Osborn, T. J., and Lister, D. H.: Updated high-resolution grids of monthly climatic observations – the CRU TS3.10 Dataset, *International Journal of Climatology*, 34, 623-642, doi:10.1002/joc.3711, 2014.
- Hugelius, G., Strauss, J., Zubrzycki, S., Harden, J. W., Schuur, E. A. G., Ping, C. L., Schirmer, L., Grosse, G., Michaelson, G. J., Koven, C. D., O'Donnell, J. A., Elberling, B., Mishra, U., Camill, P., Yu, Z., Palmtag, J., and Kuhry, P.: Estimated stocks of circumpolar permafrost carbon with quantified uncertainty ranges and identified data gaps, *Biogeosciences*, 11, 6573-6593, doi:10.5194/bg-11-6573-2014, 2014.
- Ji, D., Wang, L., Feng, J., Wu, Q., Cheng, H., Zhang, Q., Yang, J., Dong, W., Dai, Y., Gong, D., Zhang, R.-H., Wang, X., Liu, J., Moore, J. C., Chen, D., and Zhou, M.: Description and basic evaluation of Beijing Normal University Earth System Model (BNU-ESM) version 1, *Geosci. Model Dev.*, 7, 2039-2064, doi:10.5194/gmd-7-2039-2014, 2014.
- Kalnay, E., Kanamitsu, M., Kistler, R., Collins, W., Deaven, D., Gandin, L., Iredell, M., Saha, S., White, G., Woollen, J., Zhu, Y., Leetmaa, A., Reynolds, R., Chelliah, M., Ebisuzaki, W., Higgins, W., Janowiak, J., Mo, K. C., Ropelewski, C., Wang, J., Jenne, R., and Joseph, D.: The NCEP/NCAR 40-Year Reanalysis Project, *Bulletin of the American*

Meteorological Society, 77, 437-471,
doi:10.1175/1520-0477(1996)077<0437:tnyrp>2.0.co;2, 1996.

Khvorostyanov, D. V., Ciais, P., Krinner, G., Zimov, S. A., Corradi, C., and Guggenberger, G.: Vulnerability of permafrost carbon to global warming. Part II: sensitivity of permafrost carbon stock to global warming, *Tellus B*, 60, 265-275, doi:10.1111/j.1600-0889.2007.00336.x, 2008.

Koven, C., Friedlingstein, P., Ciais, P., Khvorostyanov, D., Krinner, G., and Tarnocai, C.: On the formation of high-latitude soil carbon stocks: Effects of cryoturbation and insulation by organic matter in a land surface model, *Geophysical Research Letters*, 36, L21501, doi:10.1029/2009gl040150, 2009.

Koven, C. D., Ringeval, B., Friedlingstein, P., Ciais, P., Cadule, P., Khvorostyanov, D., Krinner, G., and Tarnocai, C.: Permafrost carbon-climate feedbacks accelerate global warming, *P. Natl. Acad. Sci. USA*, 14769-14774, doi:10.1073/pnas.1103910108, 2011.

Koven, C. D., Riley, W. J., and Stern, A.: Analysis of Permafrost Thermal Dynamics and Response to Climate Change in the CMIP5 Earth System Models, *Journal of Climate*, 26, 1877-1900, doi:10.1175/jcli-d-12-00228.1, 2013.

Koven, C. D., Schuur, E. A. G., Schädel, C., Bohn, T. J., Burke, E. J., Chen, G., Chen, X., Ciais, P., Grosse, G., Harden, J. W., Hayes, D. J., Hugelius, G., Jafarov, E. E., Krinner, G., Kuhry, P., Lawrence, D. M., MacDougall, A. H., Marchenko, S. S., McGuire, A. D., Natali, S. M., Nicolsky, D. J., Olefeldt, D., Peng, S., Romanovsky, V. E., Schaefer, K. M., Strauss, J., Treat, C. C. and Turetsky, M.: A simplified, data-constrained approach to estimate the permafrost carbon-climate feedback, *Philos. Trans. A. Math. Phys. Eng. Sci.*, 373(2054), doi:10.1098/rsta.2014.0423, 2015.

Krinner, G., Viovy, N., de Noblet-Ducoudré, N., Ogée, J., Polcher, J., Friedlingstein, P., Ciais, P., Sitch, S., and Prentice, I. C.: A dynamic global vegetation model for studies of the

- coupled atmosphere-biosphere system, *Global Biogeochemical Cycles*, 19, GB1015, doi:10.1029/2003gb002199, 2005
- Lawrence, D. M., Slater, A. G., Romanovsky, V. E., and Nicolsky, D. J.: Sensitivity of a model projection of near-surface permafrost degradation to soil column depth and representation of soil organic matter, *Journal of Geophysical Research: Earth Surface*, 113, F02011, doi:10.1029/2007jf000883, 2008.
- Lawrence, D., and Slater, A.: Incorporating organic soil into a global climate model, *Clim Dyn*, 30, 145-160, doi:10.1007/s00382-007-0278-1, 2008.
- Lee, H., Swenson, S. C., Slater, A. G., and Lawrence, D. M.: Effects of excess ground ice on projections of permafrost in a warming climate, *Environmental Research Letters*, 9, 124006, doi:10.1088/1748-9326/9/12/124006, 2014.
- MacDougall, A. H., Avis, C. A., and Weaver, A. J.: Significant contribution to climate warming from the permafrost carbon feedback, *Nature Geosci.*, 5, 719-721, doi:10.1038/ngeo1573, 2012.
- McGuire, A. D., Anderson, L. G., Christensen, T. R., Dallimore, S., Guo, L., Hayes, D. J., Heimann, M., Lorenson, T. D., Macdonald, R. W., and Roulet, N.: Sensitivity of the carbon cycle in the Arctic to climate change, *Ecological Monographs*, 79, 523-555, doi:10.1890/08-2025.1, 2009.
- McGuire, A. D., Christensen, T. R., Hayes, D., Heroult, A., Euskirchen, E., Kimball, J. S., Koven, C., Lafleur, P., Miller, P. A., Oechel, W., Peylin, P., Williams, M., and Yi, Y.: An assessment of the carbon balance of Arctic tundra: comparisons among observations, process models, and atmospheric inversions, *Biogeosciences*, 9, 3185–3204, doi:10.5194/bg-9-3185-2012, 2012.
- Mitchell, T. D., and Jones, P. D.: An improved method of constructing a database of monthly climate observations and associated high-resolution grids, *International Journal of*

Climatology, 25, 693-712, doi:10.1002/joc.1181, 2005.

Nicolsky, D., Romanovsky, V., Alexeev, V., and Lawrence, D.: Improved modeling of permafrost dynamics in a GCM land-surface scheme, *Geophys. Res. Lett.*, 34, L08501, doi:10.1029/2007GL029525, 2007.

Oleson, K.W., Lawrence, D. M., Bonan, G. B., Drewniak, B., Huang, M., Koven, C. D., Levis, S., Li, F., Riley, W. J., Subin, Z. M., Swenson, S. C., Thornton, P. E., Bozbiyik, A., Fisher, R., Heald, C. L., Kluzek, E., Lamarque, J., Lawrence, P. J., Leung, L. R., Lipscomb, W., Muszala, S., Ricciuto, D. M., Sacks, W., Tang, J., Yang, Z. Technical Description of version 4.5 of the Community Land Model (CLM). P. O. Box 3000 BOULDER, COLORADO 80307-3000: National Center for Atmospheric Research. 2013 June. NCAR Technical Note #NCAR/TN-503+STR.

Osterkamp, T. E. A thermal history of permafrost in Alaska. *Proceedings of Eighth International Conference on Permafrost*, Zurich, pp. 863-868, July 21-25, 2003.

Osterkamp, T. E.: Characteristics of the recent warming of permafrost in Alaska, *Journal of Geophysical Research: Earth Surface*, 112, F02S02, doi:10.1029/2006jf000578, 2007.

Park, H., Sherstiukov. A. B., Fedorov, A. N., Polyakov, I. V., and Walsh, J. E.: An observation-based assessment of the influences of air temperature and snow depth on soil temperature in Russia, *Environmental Research Letters*, 9, 064026, doi:10.1088/1748-9326/9/6/064026, 2014.

Qian, B., Gregorich, E. G., Gameda, S., Hopkins, D. W., and Wang, X. L.: Observed soil temperature trends associated with climate change in Canada, *Journal of Geophysical Research: Atmospheres*, 116, D02106, doi:10.1029/2010jd015012, 2011.

Rawlins, M. A., Steele, M., Holland, M. M., Adam, J. C., Cherry, J. E., Francis, J. A., Groisman, P. Y., Hinzman, L. D., Huntington, T. G., Kane, D. L., Kimball, J. S., Kwok, R., Lammers, R. B., Lee, C. M., Lettenmaier, D. P., McDonald, K. C., Podest, E.,

- Pundsack, J. W., Rudels, B., Serreze, M. C., Shiklomanov, A., Skagseth, O., Troy, T. J., Vorosmarty, C. J., Wensnahan, M., Wood, E. F., Woodgate, R., Yang, D. Q., Zhang, K., and Zhang, T. J.: Analysis of the Arctic System for Freshwater Cycle Intensification: Observations and Expectations, *Journal of Climate*, 23, 5715-5737, doi:10.1175/2010jcli3421.1, 2010.
- Rawlins, M. A., McGuire, A. D., Kimball, J. S., Dass, P., Lawrence, D., Burke, E., Chen, X., Delire, C., Koven, C., MacDougall, A., Peng, S., Rinke, A., Saito, K., Zhang, W., Alkama, R., Bohn, T. J., Ciais, P., Decharme, B., Gouttevin, I., Hajima, T., Ji, D., Krinner, G., Lettenmaier, D. P., Miller, P., Moore, J. C., Smith, B., and Sueyoshi, T.: Assessment of model estimates of land-atmosphere CO₂ exchange across Northern Eurasia, *Biogeosciences*, 12, 4385-4405, doi:10.5194/bg-12-4385-2015, 2015.
- Romanovsky, V. E., Sazonova, T. S., Balobaev, V. T., Shender, N. I., and Sergueev, D. O.: Past and recent changes in air and permafrost temperatures in eastern Siberia, *Global and Planetary Change*, 56, 399-413, doi:10.1016/j.gloplacha.2006.07.022, 2007.
- Romanovsky, V. E., Smith, S. L., and Christiansen, H. H.: Permafrost thermal state in the polar Northern Hemisphere during the international polar year 2007–2009: a synthesis, *Permafrost and Periglacial Processes*, 21, 106-116, doi:10.1002/ppp.689, 2010.
- Schädel, C., Schuur, E. A. G., Bracho, R., Elberling, B., Knoblauch, C., Lee, H., Luo, Y., Shaver, G. R., and Turetsky, M. R.: Circumpolar assessment of permafrost C quality and its vulnerability over time using long-term incubation data, *Global Change Biology*, 20, 641-652, doi:10.1111/gcb.12417, 2014.
- Schaefer, K., Zhang, T., Bruhwiler, L., and Barrett, A. P.: Amount and timing of permafrost carbon release in response to climate warming, *Tellus B*, 63, 165-180, doi:10.1111/j.1600-0889.2011.00527.x, 2011.
- Schneider von Deimling, T., Meinshausen, M., Levermann, A., Huber, V., Frieler, K.,

- Lawrence, D. M., and Brovkin, V.: Estimating the near-surface permafrost-carbon feedback on global warming, *Biogeosciences*, 9, 649-665, doi:10.5194/bg-9-649-2012, 2012.
- Schuur, E. A. G., Bockheim, J., Canadell, J. G., Euskirchen, E., Field, C. B., Goryachkin, S. V., Hagemann, S., Kuhry, P., Lafleur, P. M., Lee, H., Mazhitova, G., Nelson, F. E., Rinke, A., Romanovsky, V. E., Shiklomanov, N., Tarnocai, C., Venevsky, S., Vogel, J. G., and Zimov, S. A.: Vulnerability of Permafrost Carbon to Climate Change: Implications for the Global Carbon Cycle, *BioScience*, 58, 701-714, doi:10.1641/b580807, 2008.
- Sheffield, J., Goteti, G., and Wood, E. F.: Development of a 50-Year High-Resolution Global Dataset of Meteorological Forcings for Land Surface Modeling, *Journal of Climate*, 19, 3088-3111, 10.1175/jcli3790.1, 2006.
- Slater, A. G., and Lawrence, D. M.: Diagnosing Present and Future Permafrost from Climate Models, *Journal of Climate*, 26, 5608-5623, doi:10.1175/jcli-d-12-00341.1, 2013.
- Smith, B., Prentice, I. C., and Sykes, M. T.: Representation of vegetation dynamics in the modelling of terrestrial ecosystems: comparing two contrasting approaches within European climate space, *Global Ecology and Biogeography*, 10, 621-637, doi:10.1046/j.1466-822X.2001.t01-1-00256.x, 2001.
- Smith, N. V., Saatchi, S. S. and Randerson, J. T.: Trends in high northern latitude soil freeze and thaw cycles from 1988 to 2002, *Journal of Geophysical Research-Atmospheres*, 109, D12101, doi:10.1029/2003JD004472, 2004.
- Smith, S. L., Burgess, M. M., Riseborough, D., and Mark Nixon, F.: Recent trends from Canadian permafrost thermal monitoring network sites, *Permafrost and Periglacial Processes*, 16, 19-30, doi:10.1002/ppp.511, 2005.
- Smith, S. L., Romanovsky, V. E., Lewkowicz, A. G., Burn, C. R., Allard, M., Clow, G. D.,

- Yoshikawa, K., and Throop, J.: Thermal state of permafrost in North America: a contribution to the international polar year, *Permafrost and Periglacial Processes*, 21, 117-135, doi:10.1002/ppp.690, 2010.
- Smith, S. L., Throop, J., and Lewkowicz, A. G.: Recent changes in climate and permafrost temperatures at forested and polar desert sites in northern Canada, *Canadian Journal of Earth Sciences*, 49, 914-924, doi:10.1139/e2012-019, 2012.
- Stevens, M. B., Smerdon, J. E., González-Rouco, J. F., Stieglitz, M., and Beltrami, H.: Effects of bottom boundary placement on subsurface heat storage: Implications for climate model simulations, *Geophysical Research Letters*, 34, L02702, doi:10.1029/2006gl028546, 2007.
- Troy, T. J., and Wood, E. F.: Comparison and evaluation of gridded radiation products across northern Eurasia, *Environmental Research Letters*, 4, 045008, doi:10.1088/1748-9326/4/4/045008, 2009.
- van Huissteden, J., Berrittella, C., Parmentier, F. J. W., Mi, Y., Maximov, T. C., and Dolman, A. J.: Methane emissions from permafrost thaw lakes limited by lake drainage, *Nature Clim. Change*, 1, 119-123, doi:dx.doi.org/10.1038/nclimate1101, 2011.
- Vaughan, D.G., Comiso, J.C., Allison, I., Carrasco, J., Kaser, G., Kwok, R., Mote, P., Murray, T., Paul, F., Ren, J., Rignot, E., Solomina, O., Steffen, K. and Zhang, T. (2013) *Observations: Cryosphere*. In: *Climate Change 2013: The Physical Science Basis*. Contribution of Working Group I to the Fifth Assessment Report of the Intergovernmental Panel on Climate Change [Stocker, T.F., D. Qin, G.-K. Plattner, M. Tignor, S.K. Allen, J. Boschung, A. Nauels, Y. Xia, V. Bex and P.M. Midgley (eds.)]. Cambridge University Press, Cambridge, United Kingdom and New York, NY, USA, pp. 317–382, doi:10.1017/CBO9781107415324.012.
- Watanabe, S., Hajima, T., Sudo, K., Nagashima, T., Takemura, T., Okajima, H., Nozawa, T.,

- Kawase, H., Abe, M., Yokohata, T., Ise, T., Sato, H., Kato, E., Takata, K., Emori, S., and Kawamiya, M.: MIROC-ESM 2010: model description and basic results of CMIP5-20c3m experiments, *Geosci. Model Dev.*, 4, 845-872, doi:10.5194/gmd-4-845-2011, 2011.
- Weedon, G. P., Balsamo, G., Bellouin, N., Gomes, S., Best, M. J., and Viterbo, P.: The WFDEI meteorological forcing data set: WATCH Forcing Data methodology applied to ERA-Interim reanalysis data, *Water Resources Research*, 50, 7505-7514, doi:10.1002/2014wr015638, 2014.
- Weedon, G. P., Gomes, S., Viterbo, P., Shuttleworth, W. J., Blyth, E., Österle, H., Adam, J. C., Bellouin, N., Boucher, O., and Best, M.: Creation of the WATCH Forcing Data and Its Use to Assess Global and Regional Reference Crop Evaporation over Land during the Twentieth Century, *Journal of Hydrometeorology*, 12, 823-848, doi:10.1175/2011jhm1369.1, 2011.
- Wei, Y., Liu, S., Huntzinger, D. N., Michalak, A. M., Viovy, N., Post, W. M., Schwalm, C. R., Schaefer, K., Jacobson, A. R., Lu, C., Tian, H., Ricciuto, D. M., Cook, R. B., Mao, J., and Shi, X.: The North American Carbon Program Multi-scale Synthesis and Terrestrial Model Intercomparison Project – Part 2: Environmental driver data, *Geosci. Model Dev. Discuss.*, 6, 5375-5422, doi:10.5194/gmdd-6-5375-2013, 2013.
- Westermann, S., Østby, T. I., Gislås, K., Schuler, T. V., and Etzelmüller, B.: A ground temperature map of the North Atlantic permafrost region based on remote sensing and reanalysis data, *The Cryosphere*, 9, 1303-1319, doi:10.5194/tc-9-1303-2015, 2015.
- Willmott, C. J. and K. Matsuura (2001) Terrestrial Air Temperature and Precipitation: Monthly and Annual Time Series (1950 - 1999), http://climate.geog.udel.edu/~climate/html_pages/README.ghcn_ts2.html.
- Zhang, T., Barry, R., Gilichinsky, D., Bykhovets, S. S., Sorokovikov, V. A., and Ye, J.: An

792 Amplified Signal of Climatic Change in Soil Temperatures during the Last Century at
793 Irkutsk, Russia, *Climatic Change*, 49, 41-76, doi:10.1023/a:1010790203146, 2001.
794

795 Table 1. Soil depth for soil thermal dynamics and climate forcing used in each model.

796

Model	Soil depth (m)	Soil discretization layers	Bottom boundary geothermal heat flux (mW m ⁻²)	Climate forcing (Reference)	Model reference	Note
CLM	45.1	30	0	CRUNCEP v4 (http://dods.extra.cea.fr/)	Oleson et al., 2013	
CoLM	3.4	10	0	Princeton (Sheffield et al., 2006)	Dai et al., 2003, 2004	
ISBA	12.0	14	0	WATCH (1901-1978) WFDEI (1978-2009) (Weedon et al., 2011; 2014)	Decharme et al., 2011, 2013	
JULES	20.8	16	0	WATCH (1901-2001) (Weedon et al., 2011)	Best et al., 2011; Clark et al., 2011	
LPI-GUESS	3.0	8	0	CRU TS 3.1 (Harris et al., 2014)	Smith et al., 2001; McGuire et al., 2012	Soil temperature in the top 3 meter is based on another 6 padding layers (10 meter) below as the bottom layer condition. Surface shortwave downward radiation was calculated from cloudiness data set; No longwave downward radiation and vapor pressure were used.
MIROC-ESM	14.0	6	0	CMIP5 Drivers (Watanabe et al., 2011)	Watanabe et al., 2011	
ORCHIDEE	47.4	32	58	WATCH (1901-1978) WFDEI (1978-2009) (Weedon et al., 2011; 2014)	Krinner et al., 2005; Koven et al., 2011; Gouttevin et al., 2012	
UVic	250.3	14	0	CRUNCEP v4 (http://dods.extra.cea.fr/)	Avis et al., 2011, MacDougall et al., 2012	Surface shortwave and longwave downward radiation were internally Calculated.

				temperature from CRU TS3.1, precipitation from UDel, wind speed from NCEP-NCAR (Mitchell and Jones, 2005; Willmott and Matsura, 2001; Adam et al., 2006; Kalnay et al., 1996)		797
UW-VIC	25.0	25	0		Bohn et al., 2013	Surface shortwave and longwave downward radiation were internally Calculated.

798 Table 2. Description of simulations used in this study.

799

Simulation ID	Climate	CO ₂
R01	variable	variable
R02	variable, but with detrended T _a	variable
R03	variable	constant in the year of 1960
R04	variable, but with detrended T _a and precipitation	variable
R05	variable, but with detrended T _a and LWDR	variable
R06	variable, but with detrended T _a , precipitation and LWDR	variable

800

801

802 Table 3. The trends of annual air temperature (T_a), precipitation and longwave downward radiation (LWDR) in the second to fourth columns. The
803 fifth column shows the trends of annual T_s at 20 cm in the reference simulation (R01). The last four columns show the contributions of drivers
804 (T_a , precipitation, CO_2 and LWDR) on the trend of T_s as mentioned in Methods section. The relative contributions (divided by the trend of T_s in
805 Ref) are shown in the parentheses. The bold font indicates statistically significant ($P < 0.05$).

Model	Trend of T_a ($^{\circ}C\ yr^{-1}$)	Trend of precipitation ($mm\ yr^{-2}$)	Trend of LWDR ($W\ m^{-2}\ yr^{-1}$)	Simulated Trend of T_s (R01) ($^{\circ}C\ yr^{-1}$)	Contribution from T_a (R01-R02) ($^{\circ}C\ yr^{-1}$)	Contribution from precipitation (R02-R04) ($^{\circ}C\ yr^{-1}$)	Contribution from CO_2 (R01-R03) ($^{\circ}C\ yr^{-1}$)	Contribution from LWDR (R02-R05) ($^{\circ}C\ yr^{-1}$)
CLM	0.031	0.13	0.114	0.016(100%)	0.015(92%)	-0.002(-12%)	0.001(4%)	-
CoLM	0.031	-0.05	0.058	0.010(100%)	-	-	-	-
ISBA	0.033	-0.17	0.183	0.030(100%)	0.030(99%)	0.001(2%)	0.000(-1%)	-
JULES	0.034	0.31	0.189	0.017(100%)	-0.001(-6%)	-0.005(-28%)	0.000(0%)	0.005(31%)
LPJ-GUESS	0.033	0.11		0.026(100%)	0.018(67%)	0.000(-1%)	-0.001(-5%)	-
MIROC-ESM	0.025	0.44	0.140	0.024(100%)	-	-	-	-
ORCHIDEE	0.045	0.00	0.201	0.030(100%)	0.010(34%)	0.002(7%)	0.001(2%)	0.017(56%)
UVic	0.031	0.11		0.031(100%)	0.017(56%)	0.000(0%)	0.000(-1%)	-
UW-VIC	0.031	2.01	0.125	0.011(100%)	0.029(266%)	-0.005(-47%)	0.000(0%)	-

Figure legends

Figure 1. The spatial extent of regions defined in this study. Red, green, blue and magenta indicate the regions of boreal North America (BONA), boreal Europe (BOEU) and boreal Asia (BOAS), other permafrost areas (Other), respectively. We only selected BONA, BOEU and BOAS sub-regions for analysis in this study.

Figure 2. Simulated anomaly of annual T_s at 20 cm averaged over boreal regions of each model, during the period of 1960-2000.

Figure 3. Simulated trends of annual T_s at 20 cm averaged over boreal regions and sub-regions of each model, from 1960 to 2000. * indicates significant trend of T_s ($P < 0.05$).

Figure 4. Spatial distributions of trends of annual T_s at 20 cm over boreal regions from 1960 to 2000 in (a) CLM, (b) CoLM, (c) ISBA, (d) JULES, (e) LPJ-GUESS, (f) MICRO-ESM, (g) ORCHIDEE, (h) UVic and (i) UW-VIC models. The black dots indicate regions with significant trends of T_s ($P < 0.05$). Note that extreme values outside of the range of $-0.06 \text{ }^{\circ}\text{C yr}^{-1}$ - $0.06 \text{ }^{\circ}\text{C yr}^{-1}$ are shown in deepest blue and red in the color bar.

Figure 5. Simulated trends of annual T_s over boreal regions as a function of soil depths (a) 0 - 3 m and (b) 0 - 40 m for the nine models. Note the different total soil depths of the models and negative trends for UW-VIC (~ -0.01 - $-0.03 \text{ }^{\circ}\text{C yr}^{-1}$) below 2.3 m are not shown in the plots.

Figure 6. Spatial distributions of difference in trends of annual T_s at 0.2 m and 3 m over boreal regions from 1960 to 2000 in (a) CLM, (b) CoLM, (c) ISBA, (d) JULES, (e) LPJ-GUESS, (f) MICRO-ESM, (g) ORCHIDEE, (h) UVic and (i) UW-VIC models. The black dots indicate statistically significant difference by t-test ($P < 0.05$). Note that extreme values outside of the range of $-0.015 \text{ }^{\circ}\text{C yr}^{-1}$ - $0.015 \text{ }^{\circ}\text{C yr}^{-1}$ are shown in deepest

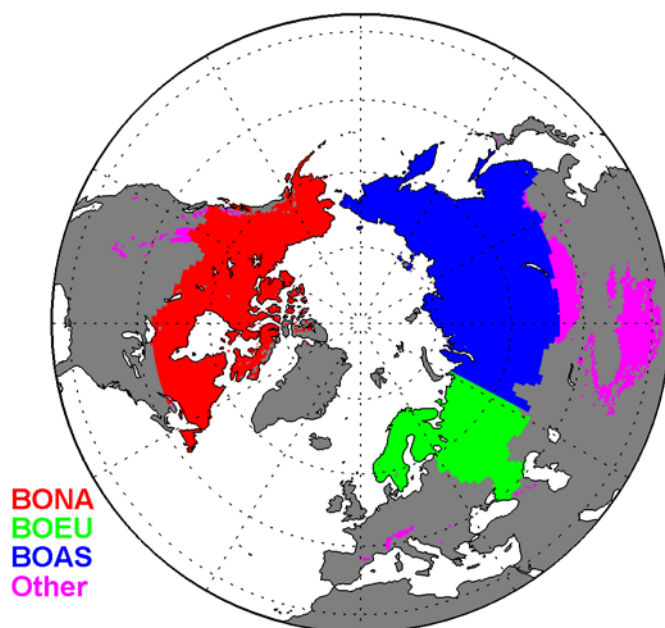
blue and red in the color bar.

Figure 7. Simulated trends of annual T_s at 20 cm and T_a in the climate forcing data across the nine models.

Figure 8. (a) Simulated trends of annual T_s at 20 cm and annual LWDR in the climate forcing data over boreal regions across the seven models which used and provided LWDR in their climate forcing. The thin black dotted lines indicate the linear regression and 95% confidence interval. The gray dashed line with double arrows indicates the uncertainty of trend of LWDR in the climate forcing data. The solid blue and orange lines with double arrows indicate FU and SU, respectively. The red solid vertical line with shade area shows the trend of LWDR ($0.087 \pm 0.023 \text{ W m}^{-2} \text{ yr}^{-1}$) during the period 1960-2000 from CRUNCEP v5.2 dataset. The purple solid vertical line with shade area shows the trend of LWDR ($0.187 \pm 0.028 \text{ W m}^{-2} \text{ yr}^{-1}$) during the period 1960-2000 from WATCH dataset. (b) The prior normal probability density function (PDF) with modeled mean and standard deviation (black solid line) of trend of T_s at 20 cm and posterior normal PDF of trend of annual T_s at 20 cm with given trend of LWDR (red dotted line) from CRUNCEP and WATCH (purple dotted line) respectively.

Figure 9. Simulated trends of summer T_s at 1 m and loss rate of NSPA over (a) boreal regions, (b) BONA, (c) BOEU and (d) BOAS across the nine models.

853 Figure 1. The spatial extent of regions defined in this study. Red, green, blue and magenta
854 indicate the regions of boreal North America (BONA), boreal Europe (BOEU) and boreal
855 Asia (BOAS), other permafrost areas (Other), respectively. We only selected BONA, BOEU
856 and BOAS sub-regions for analysis in this study.



857

858

Figure 2. Simulated anomaly of annual T_s at 20 cm averaged over boreal regions of each model, during the period of 1960-2000.

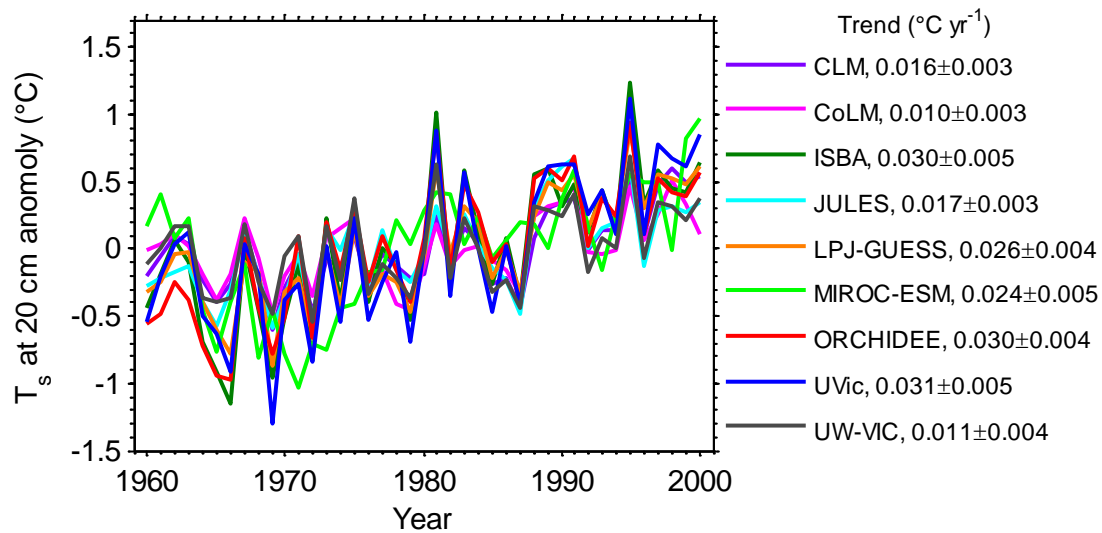


Figure 3. Simulated trends of annual T_s at 20 cm averaged over boreal regions and sub-regions of each model, from 1960 to 2000. * indicates significant trend of T_s ($P < 0.05$).

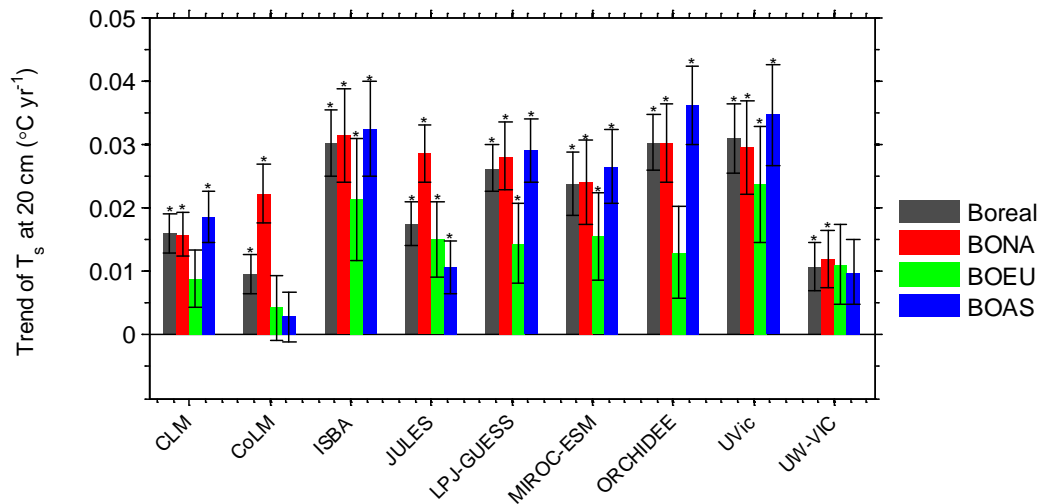


Figure 4. Spatial distributions of trends of annual T_s at 20 cm over boreal regions from 1960 to 2000 in (a) CLM, (b) CoLM, (c) ISBA, (d) JULES, (e) LPJ-GUESS, (f) MICRO-ESM, (g) ORCHIDEE, (h) UVic and (i) UW-VIC models. The black dots indicate regions with significant trends of T_s ($P < 0.05$). Note that extreme values outside of the range of -0.06 $^{\circ}\text{C yr}^{-1}$ - 0.06 $^{\circ}\text{C yr}^{-1}$ are shown in deepest blue and red in the color bar.

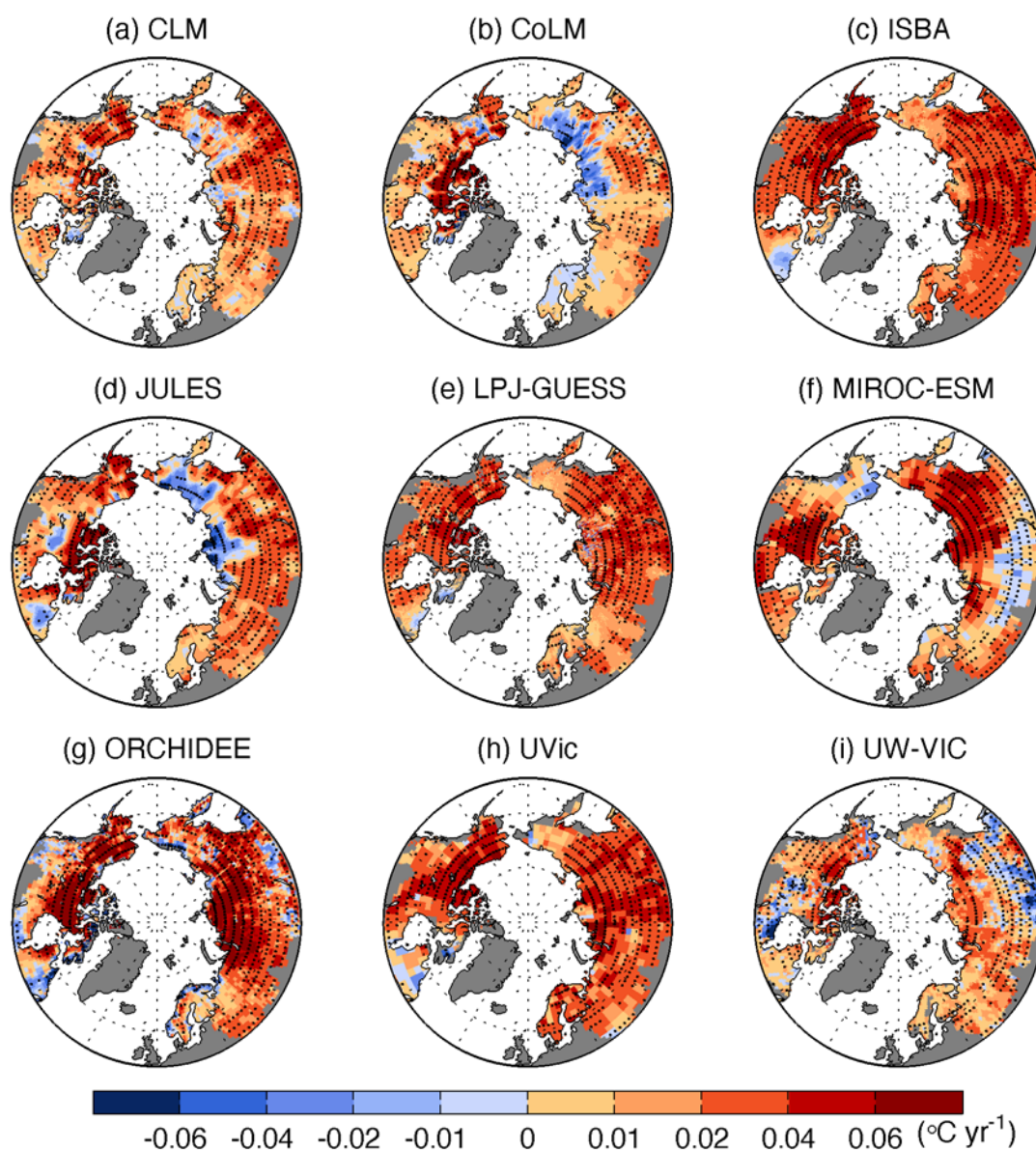


Figure 5. Simulated trends of annual T_s over boreal regions as a function of soil depths (a) 0 - 3 m and (b) 0 - 40 m for the nine models. Note the different total soil depths of the models and negative trends for UW-VIC (~ -0.01 - -0.03 $^{\circ}\text{C yr}^{-1}$) below 2.3 m are not shown in the plots.

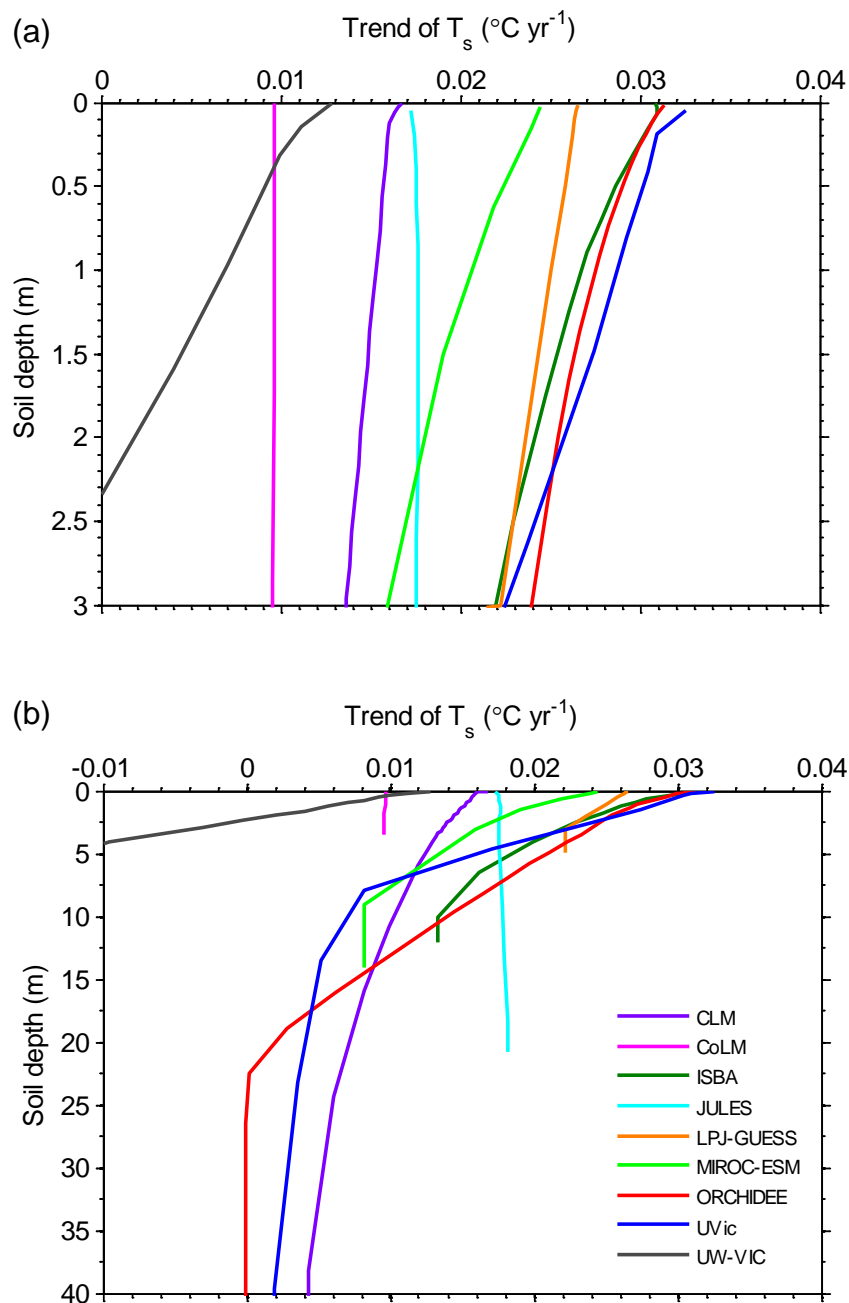


Figure 6. Spatial distributions of difference in trends of annual T_s at 0.2 m and 3 m over boreal regions from 1960 to 2000 in (a) CLM, (b) CoLM, (c) ISBA, (d) JULES, (e) LPJ-GUESS, (f) MICRO-ESM, (g) ORCHIDEE, (h) UVic and (i) UW-VIC models. The black dots indicate statistically significant difference by t-test ($P < 0.05$). Note that extreme values outside of the range of $-0.015 \text{ } ^\circ\text{C yr}^{-1}$ - $0.015 \text{ } ^\circ\text{C yr}^{-1}$ are shown in deepest blue and red in the color bar.

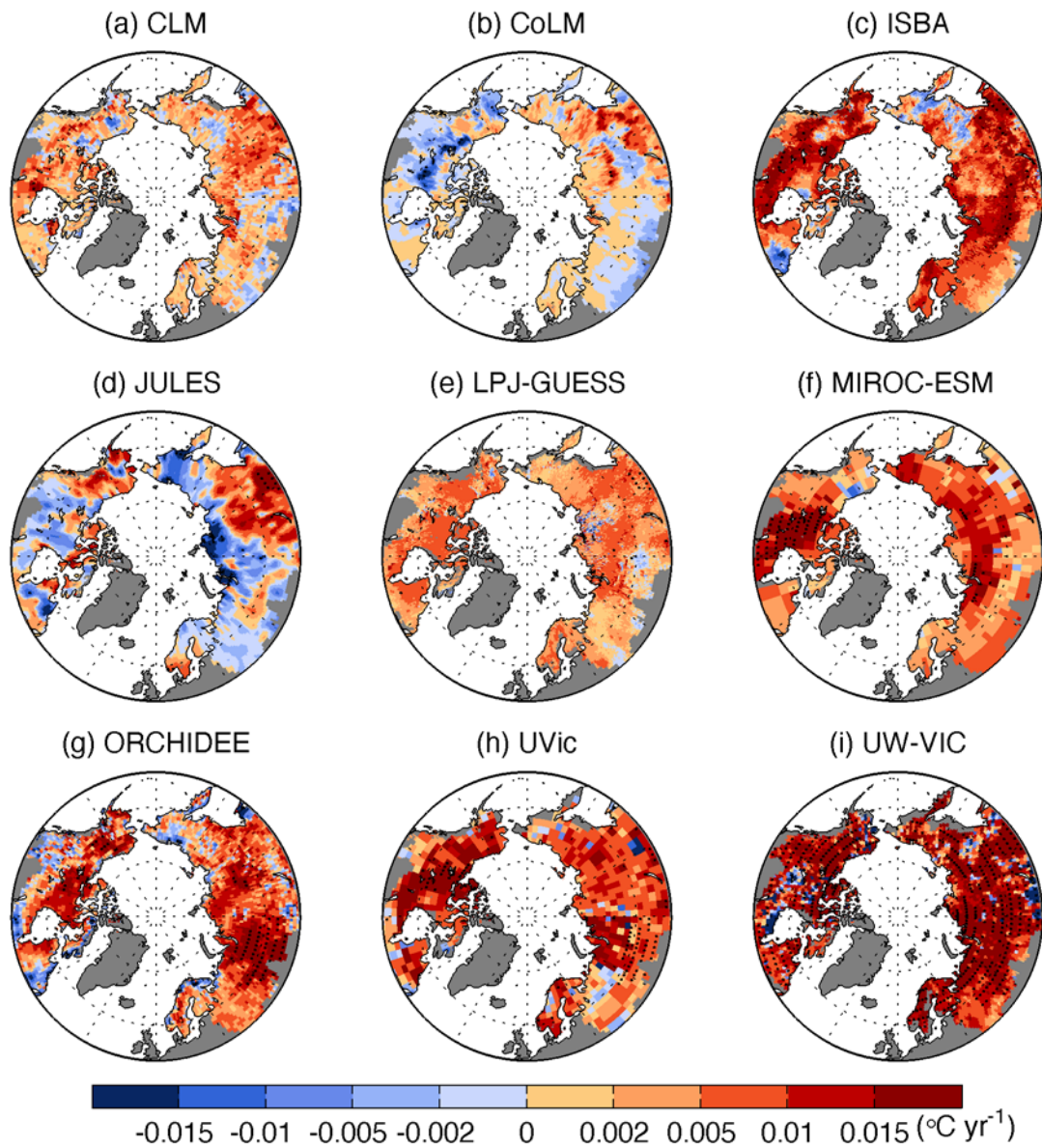


Figure 7. Simulated trends of annual T_s at 20 cm and T_a in the climate forcing data across the nine models.

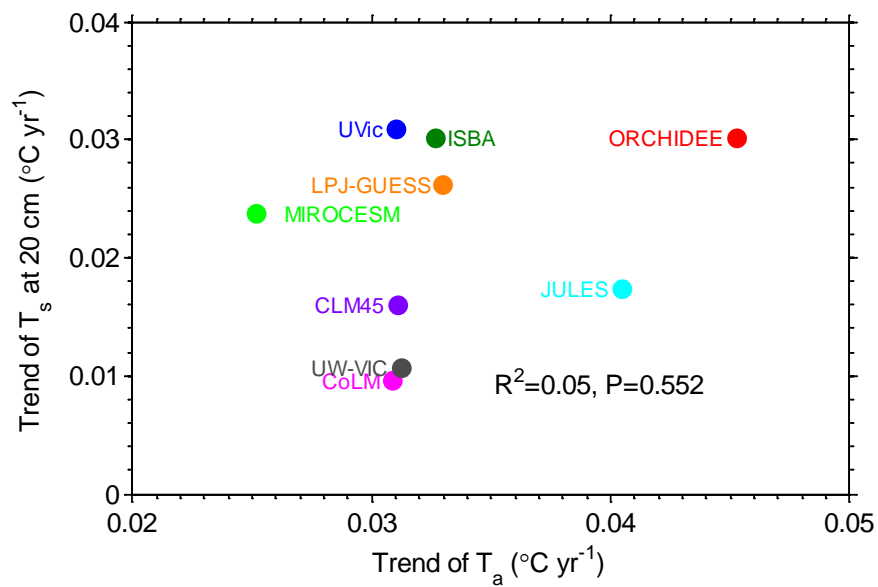


Figure 8. (a) Simulated trends of annual T_s at 20 cm and annual LWDR in the climate forcing data over boreal regions across the seven models which used and provided LWDR in their climate forcing. The thin black dotted lines indicate the linear regression and 95% confidence interval. The gray dashed line with double arrows indicates the uncertainty of trend of LWDR in the climate forcing data. The solid blue and orange lines with double arrows indicate FU and SU, respectively. The red solid vertical line with shade area shows the trend of LWDR ($0.087 \pm 0.023 \text{ W m}^{-2} \text{ yr}^{-1}$) during the period 1960-2000 from CRUNCEP v5.2 dataset. The purple solid vertical line with shade area shows the trend of LWDR ($0.187 \pm 0.028 \text{ W m}^{-2} \text{ yr}^{-1}$) during the period 1960-2000 from WATCH dataset. (b) The prior normal probability density function (PDF) with modeled mean and standard deviation (black solid line) of trend of T_s at 20 cm and posterior normal PDF of trend of annual T_s at 20 cm with given trend of LWDR (red dotted line) from CRUNCEP and WATCH (purple dotted line) respectively.

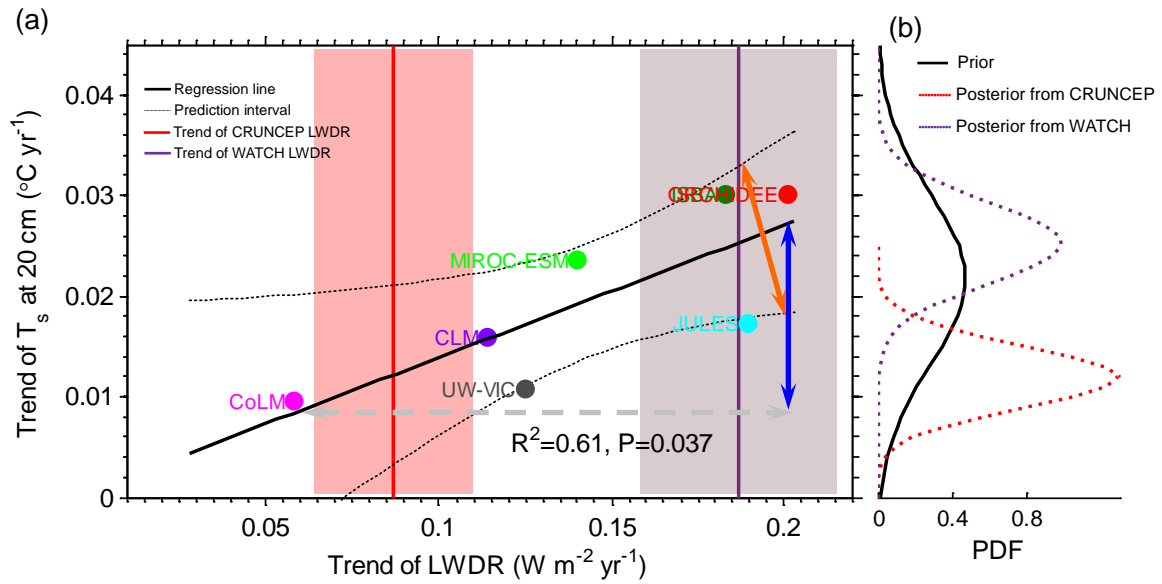


Figure 9. Simulated trends of summer T_s at 1 m and loss rate of NSPA over (a) boreal regions,
 (b) BONA, (c) BOEU and (d) BOAS across the nine models.

